SAND2015-10833C

Volumetric Measurement of Transonic Cavity Flow Using Stereoscopic Particle Image Velcimetry

Edward P. DeMauro* Steven J. Beresh† Justin L. Wagner‡ John F. Henfling §

and Russel W. Spillers¶

Sandia National Laboratories, Albuquerque, NM 87111, USA

Stereoscopic particle image velocimetry was used to experimentally measure the recirculating flow within finite-span cavities of varying complex geometry at a freestream Mach number of 0.8. Volumetric measurements were made to investigate the edge-effect influences. Each of the geometries could be classified as being an open-cavity, based on L/D. The addition of ramps altered the recirculation zone within the cavity, causing it to move along the streamwise direction. Within the simple rectangular cavity, a system of counter-rotating streamwise vortices formed due to spillage from along the side wall, which caused for the separated mixing layer to develop a steady spanwise waviness. The ramped complex geometry, due to the presence of leading edge and side ramps, appeared to suppress the formation of streamwise vorticity associated with side wall spillage, resulting in a much more two-dimensional mixing layer.

Nomenclature

b	Cavity span (m)
D	Cavity depth (m)
L	Cavity length (m)
M_∞	Freestream Mach number
P_0	Tunnel stagnation pressure (kPa)
T_0	Tunnel stagnation temperature (K)
t	Time (s)
U	Time-averaged streamwise velocity (m/s)
U_∞	Freestream velocity (m/s)
V	Time-averaged wall-normal velocity (m/s)
V_{tot}	Time-averaged total velocity (m/s)
W	Time-averaged spanwise velocity (m/s)
x	Streamwise direction (m)
y	Wall-normal direction (m)
z	Spanwise direction (m)

*Postdoctoral Appointee, Engineering Sciences Center, P.O. Box 5800, MS-0825, Albuquerque, NM 87125, Member AIAA. Corresponding author: epdemau@sandia.gov

†Distinguished Member of the Technical Staff, Engineering Sciences Center, P.O. Box 5800, MS-0825, Albuquerque, NM 87125, Associate Fellow AIAA.

‡Senior Member of the Technical Staff, Engineering Sciences Center, P.O. Box 5800, MS-0825, Albuquerque, NM 87125, Member AIAA.

§Principal Technologist

¶Senior Technologist

I. Introduction

Compressible flow over an open cavity has been an area of interest for years, primarily due to store separation from an aircraft bay. At the leading edge of a cavity, a free shear layer is formed that may travel the length of the cavity. As identified by Tracy & Plentovich,[1] subsonic and transonic cavities may be termed *open*, *closed*, or *transitional* depending on the relative location of the mixing layer with respect to the floor of the cavity. In this sense, the open regime is categorized by the separated mixing layer impinging on the trailing edge of the cavity. This impingement of the mixing layer results in pressure waves that may propagate back upstream and resonate with the mixing layer instability, resulting in a feedback mechanism and acoustic disturbances known as the Rossiter tones.[2] In general, the open-cavity is associated with a length-to-depth ratio, $L/D <$ 6-8. In contrast, a closed-cavity is one where the mixing layer instead impinges on the floor of the cavity, which may or may not result in some type of resonance, and is associated with larger length-to-depth ratios.[1]

The overarching thrust towards understanding this particular type of flow can be appreciated when considering its applications. It was shown by Coley & Lofthouse[3] that a store within the cavity did little to alter the observed dominant frequencies; however, as indicated by Wagner et al.,[4] the Rossiter tones may resonate with the natural frequencies of the store itself. Although the semi-empirical relationship put forth by Rossiter[2] and later modified by Heller & Bliss[5] can identify the relevant frequencies associated with flow over an open cavity, it cannot determine their amplitudes. Dix & Bauer[6] attempted to address this shortcoming within the literature by developing an analytical model to approximate the amplitudes. Furthermore, Casper et al.[7] demonstrated that both the amplitudes and the predicted frequencies can be altered by changes to the geometry of the cavity.

These results echo findings from many other researchers that demonstrate that the anticipated cavity tones can be altered to a degree by increasing three-dimensionalities within the cavity. Ahuja & Mendoza,[8] for example, demonstrated the sensitivity of tonal amplitudes to the length-to-width ratio, L/b, showing that the amplitudes decreased proportionally to the increase in this ratio. Disimile et al.[9] provided further evidence of the importance of L/b by measuring a redistribution of energy across tonal modes associated with increasing ratio; i.e. they found an increase in the number of dominant frequencies within their unsteady pressure power spectra. Hein et al.[10] used simulations to study the effect of two- vs. three-dimensional cavities, and the impact that confinement within a wind tunnel would have on the resulting acoustics. They noted that confinement tends to dampen acoustic amplitudes, while also seeing an increased level of acoustic radiation losses for three-dimensional cavities in comparison to two-dimensional cavities. Woo et al.[11] showed that variation of the width-to-depth ratio resulted in changes to the dominant frequencies within the cavity. In addition, to these, work by Larchevêque et al.[12] and Brès & Colonius[13] have shown that spanwise instabilities can modulate the amplitudes of the Rossiter tones.

Unfortunately, many studies are limited in their overall approximation of real-world scenarios as experiments oftentimes attempt to mitigate the effect of three-dimensionalities and study the mixing layer feedback mechanism divorced of any type of sidewall effects. In addition, the simplified geometry of a rectangular cavity does not accurately represent the more complicated flow features associated with the storage bay on the underside of an aircraft. This study is a continuation of the work performed by Casper et al.,[7] which attempted to address these apparent shortcomings within the literature by investigating the unsteady pressure field associated with a *complex geometry*, i.e. a series of geometries of finite width designed to better approximate the underbelly of an aircraft. In this present study, the cavity flow fields corresponding to the unsteady measurements of Casper et al.[7] were investigated using stereoscopic particle image velocimetry in order to understand the impact that these complex geometries may have on the overall flow within the cavity.

II. Experimental Setup

Experiments were conducted at Sandia National Laboratories' Trisonic Wind Tunnel (TWT) facility, using a blowdown-to-atmosphere wind tunnel with a rectangular test section measuring 305 mm $\times$ 305 mm, enclosed within a pressurized plenum. To mitigate the effect of acoustic resonance due to the test section duct mode, porous walls were employed for the upper surface and a single side surface.[15] The experiments were performed at a freestream Mach number, $M_\infty = 0.8$; the stagnation pressure and temperature of the tunnel were held at constant values: $P_0 = 112$ kPa and $T_0 = 321 \pm 2$ K, respectively, with the test section

walls at a temperature of 307 ± 3 K. These conditions corresponded to a freestream velocity of $U_\infty = 271$ m/s, measured at the entrance of the test section, resulting in an experimental Reynolds number of $\frac{Re_L}{L} = 18.9 \cdot 10^6/\text{m}$.

The complex cavity hardware is formed from a rectangular cavity mounted such that its upper surface was flush with the tunnel floor. The dimensions of the rectangular cavity are $L = 203.2$ mm, $D = 29$ mm, and $b = 101.6$ mm, resulting in $L/D = 7$ and $L/b = 2$. The various complex geometries are modifications of this initial rectangular cavity, created by adding a number of different components to the front and side edges of the cavity (Fig. 1). These features are designed to approximate the flight geometry of a realistic aircraft bay by adding non-uniformities to the incoming flow through the use of ramped surfaces. For ease of manufacturing, flat surfaces with angles (which better represent real aircraft geometry) were used instead of curves surfaces. Care was taken in the design of these ramped elements to ensure that angles were below limits for incipient separation.[7]

The baseline complex cavity (Fig. 1b) by the addition of a smooth ramp, inclined at an angle of 5.7°, which raises the leading edge of the cavity 12.7 mm above the trailing edge. Two side ramps are also added to the baseline complex cavity in order to provide for a smooth transition from this elevated leading edge to the trailing edge height. It should be noted here that the side ramps have angles of 26.6° in the spanwise direction. The baseline complex cavity, therefore has a streamwise variation in L/D with a value of 7 at its leading edge, decreasing to 4.9 at the trailing edge.

Modification of the leading edge ramp on the baseline complex cavity leads to the centered scoop configuration (Fig. 1c). The purpose of the scoop is to approximate influence of the engine inlet on the oncoming flow over the cavity. As flow by-passes the engine inlet, it can travel down a shallow channel leading into the bay. Furthermore, this flow passes over a jagged leading edge that over-hangs into the weapons bay, which is modeled in the scoop and tooth complex cavity (Fig. 1d).

The tunnel was seeded using a Corona Vi-Count 5000 thermal smoke generator, which produced 0.2-0.3 μm particles from a mineral oil base. Smoke particles were released into the stagnation chamber of the *TWT*, in order to dissipate disturbances introduced by the particle injectors. Particles measured in situ were found to be between 0.7-0.8 μm due to agglomeration, resulting in an estimated Stokes number of 0.02. The light source was a 400 mJ frequency-doubled dual cavity Spectra Physics PIV-400 Nd:YAG laser, which produced a 1.5 mm thick, 532 nm wavelength laser sheet.

Stereoscopic particle image velocimetry (*SPIV*) was used to measure the flow field at the center plane of the cavity, as shown in Fig. 2, which also identifies the data coordinate axes. Experiments were conducted according to the setup described by Beresh et al.[16,17] using two commercial LaVision DaVis 8.2 systems, simultaneously. Images were obtained using four LaVision Imager sCMOS cameras with 200 mm lenses and Scheimpflug adapters, each with a resolution of 2560 × 2160 pixels, digitized at 16 bits: two cameras were used to capture the upstream portion of the measurement domain, two the downstream portion. Image pairs were acquired with a time delay between laser pulses of $\delta t = 1.4$ μs.

SPIV calibration was performed using a single level 101.6 × 101.6 mm calibration target, which had a square grid of dots spaced 6.35 mm apart. The target was initially positioned at the spanwise centerline of the cavity. The target was mounted on a linear stage that allowed for calibration images to be taken at 7 different spanwise locations (based on the axes in Fig. 2), in increments of 0.25 mm, at $z/D = 0$, ±0.009, ±0.017, and ±0.026.

The camera mounting and traverse mechanism are shown in Fig. 3a and b. In order to view into each of the cavities within the constraints of *TWT*'s optical access, a mirror was used to reflect light scattered from the seed particles into the cameras, as seen in Fig. 3c. The cameras were mounted such that each system had a stereo-angle of about 28°, inclusively (half angle of about 14°), with a tilt angle of about 40°. The cameras were mounted onto two Newport M-UMR8.51 (two per stage) linear translation stages (51 mm of travel), each operated with a BM17.51 micrometers (accurate to within 10 μm). Fluid volumes were measured by collecting *SPIV* measurements at multiple spanwise locations ($z/D = 0$, -0.07, -0.14, -0.21, -0.28, -0.34, -0.41, -0.55, -0.69, -0.83, -0.97, -1.10, -1.17, -1.24, -1.31, -1.38, and -1.45).

SPIV data were processed using a multi-pass method with an initial pass using 64 × 64 pixel interrogation windows, followed by two passes using 32 × 32 pixel interrogation windows, with a 50% overlap. Prior to vector processing, a stereoscopic self-calibration procedure was performed in order to remove disparity vectors associated with slight misalignment of the laser sheet with the calibration target. The resulting vector resolutions were 0.45 mm/vector and 0.48 mm/vector. The precision uncertainty of mean velocity components were determined from $\varepsilon_p = 2\sigma/\sqrt{N}$, where σ is the standard deviation of each velocity com-

ponent and N is the total number of instantaneous vectors in an average. An estimation of the precision error (across 900 vectors) was obtained from a single downstream spanwise location where local turbulent kinetic energy was observed to be largest, in the rectangular cavity. Within the shear layer, where standard deviations were seen to be largest, a conservative estimate of the precision errors for U, V, and W were $0.009U_\infty$, $0.008U_\infty$, and $0.009U_\infty$, respectively.

III. Results/Discussion

III.A. *SPIV* measurement of cavity flows at center plane

As previously mentioned, the Rossiter tones are formed from the free shear layer issuing from the upstream leading edge, impinging on the downstream wall. The resulting velocity fields for four configurations (rectangular cavity, baseline cavity, center scoop cavity, and center scoop cavity with tooth) are shown in Fig. 4, represented by color contours of V_{tot} with in-plane streamlines, at $x/D = 0$. These vector fields were formed from the average of 3000 instantaneous image pairs. In each configuration, the separated mixing layer spreads with increasing streamwise distance. Comparing the baseline complex cavity (Fig. 4b) to the rectangular cavity (Fig. 4a), the leading edge ramp on the baseline complex cavity elevates the separated mixing layer from $y/D \approx 0$ to $\sim$0.5, due to the elevated leading edge. The center scoop has the effect of lowering the mixing layer again (Fig. 4c), and this effect continues with the presence of the tooth (Fig. 4d), both associated with the leading edge being lowered again at centerline.

The rectangular cavity (Fig. 4a), along with the center scoop complex cavity (Fig. 4c) exhibit signs of a *rear vortex*, due to the presence of two distinct recirculation zones; a primary located at $x/D \approx 3$, and a secondary at $x/D \approx 5.5$ - 6. This type of vortical structure, observed by Crook et al. in a low-speed subsonic cavity of similar dimensions, rotates with the same sense as the main recirculation zone.[18] Furthermore, Crook et al. reported measuring a rear vortex in their experiment that occupied $\sim$20% of the cavity length, which is similar to the size of the rear vortex seen in rectangular cavity (Fig. 4a).[18]

In contrast to the rectangular cavity, the baseline complex cavity, shown in Fig. 4b, has a single, large recirculation zone at $x/D \approx 4.25$. The baseline complex cavity has an elevated leading edge in comparison to the rectangular case, resulting in an effective decrease in aspect ratio ($L/D = 4.9$). The center scoop (Fig. 4c), on the other hand, once again shifts the leading edge of the cavity, downward in the vertical direction at the center plane. This lowered leading edge increases the local L/D to 5.4 at centerline, recovering the rear vortex, albeit smaller than that observed in the rectangular cavity. It is important to note here that the scooped cut-out provides an additional source of three-dimensionality that will be the subject of future investigation, as it is not detectable solely from the center plane.

Regarding the scoop with tooth complex cavity (Fig. 4d), it appears that the cavity flow is representative of a closed-cavity regime, indicated by the presence of an upwash at $x/D < 2.5$, which also seems to indicate flow traveling in the streamwise direction along the floor of the cavity.[1] However, the complexity of this cavity is enhanced due to the fact that the tooth is suspended over the cavity floor some distance from the location of the leading edge of the rectangular cavity. While this does indeed change the effective L/D, it is not readily apparent whether or not this flow can be properly termed open or closed, due to the fact that the cavity itself is partially enclosed.

Excluding the scoop with tooth complex cavity for the reasons mentioned, all cavities shown appear to be representative of an open-cavity regime, resembling the results of Murray et al.,[20] with the aspect ration of the rectangular cavity being $L/D = 7$, within the upper limit of the open-cavity regime.[1] It is important to note that these regimes are defined for two-dimensional cavities in the absence of spillage from side walls. The presence of the side-wash may draw the mixing layer towards the cavity floor, resulting in the cross-over into a transitional regime to occur at smaller values of L/D. Evidence of this type of three-dimensionality was shown by Beresh et al.,[16,17] who identified regions of high *TKE* located along the side walls of their cavities. Indeed, these regions grew in size with increasing streamwise distance along the length of the cavity, and indicated the presence of increased turbulent mixing. In addition, Arunajatesan et al.[19] showed that the influence of spillage from the side walls depended on the ratio of L/b (1.0, 1.67, 5.0); they noted in particular that their simulation at $L/b = 1.67$ showed strong spanwise three-dimensionality induced by spillage vortices.

III.B. Cross-stream distributions of U at center plane

To better appreciate the differences between the various configurations, wall-normal distributions of streamwise velocity are shown in Fig. 5, for the four geometries, at x/D = 2.5, 3.0, 3.5, 4.0, 4.5, and 5.0. The velocity profiles each resemble a hyperbolic tangent profile. Due to the variable location of the leading-edge, the inflection points in each subplot move along y/D as a function of configuration and streamwise distance.

In each configuration, the vertical location of zero velocity shifts downwards along the wall-normal axis; likewise, the inflection points in the mixing layers move continually upwards. This trend indicates a spreading of the mixing layer with streamwise direction. Along with this, it is evident that the rear wall of the cavity creates a back-pressure, resulting in a streamwise adverse pressure gradient that decelerates the flow as it approaches the rear wall. The presence of such an adverse pressure gradient is also evident from the increasing values of reverse flow with decreasing streamwise direction. The baseline complex cavity (Fig. 5b), however, has a greater degree of flow deceleration, due to the presence of the large recirculation zone observed in this cavity (Fig. 4b).

III.C. Volumetric measurement of the cavity

Inherent in all of the cavity morphologies is a degree of three-dimensionality. This is present even in the rectangular cavity, where the sharp walls may induce vorticity as flow is drawn over the side walls to the low pressure region within the cavity. However, within the literature, few studies have been performed which have investigated these three-dimensionalities experimentally. Crook et al.[18] made measurements in water using multiple 2C *PIV* planes in various orientations, exploring the flow topology. Likewise, Haigermoser et al. used tomographic *PIV* to make flow field measurements within deep rectangular[21] and circular cavities,[22] albeit in low-speed flows. To investigate these three-dimensionalities, the experiment was repeated at 17 spanwise locations, in increments of 2 or 4 mm, depending on proximity to the centerline or wall. The total data collected for two of the cavities (rectangular and baseline complex) are shown in Fig. 6, along with their associated interpolated volumes. Each plane represents the average of 900 image pairs. Taking these data, an inverse-distance interpolation was performed in Tecplot, resulting in volumetric measurements of the cavity flows ($2.5 \leq x/D \leq 6.5$, $-0.95 \leq y/D \leq 1.2$, $-1.45 \leq z/D \leq 0$). Note that the cavity has a width of $b/D = 3.5$; therefore *SPIV* measurements do not extend out to z/D = -1.75 due to limitations on optical access. For these preliminary results, the planes were interpolated onto a uniform grid in increments of 2 mm in the spanwise direction.

As was seen in Fig. 4, the volumes in Fig. 6 show that the 5.7° ramp lifts the mixing layer in the wall-normal direction, in comparison with the rectangular cavity, resulting in a larger recirculation zone. Although it is not possible to determine reverse flow from V_{tot}, the recirculation zone inferred here from the region of dark blue contours shown in Fig. 6, which indicate where velocity is locally zero. This will be revisited later. In both cases, the *SPIV* measurements reveal that the cavity flow displays a surprising degree of two-dimensionality; this is slightly misleading as the iso-contours shown in Fig. 6 extend above the separated mixing layer ($y/D > 0$), where much of the effect of the presence of the cavity is limited to acceleration of streamwise velocity about the mixing layer.

To better explain the complex three-dimensionalities present in Fig. 6, the following subsections will look at slices taken in various orientations within these fluid volumes. Important flow features will be discussed, with the final subsection summarizing and unifying these findings into a discussion on the streamwise vorticity within each cavity.

III.C.1. Slices of spanwise vorticity (ω_z)

The complex interaction of the spillage from along the edges of the cavity with the separated mixing layer issuing from the leading edge of the cavity can best be appreciated by looking at plane slices within the fluid volumes. Spanwise slices of spanwise vorticity with in-plane streamlines are shown in Fig. 7 for three separate locations: z/D = 0, -0.72, and -1.38. In comparison with Fig. 4a and b, the data shows a large degree of repeatability. At centerline, the rectangular cavity (Fig. 7c) once again shows a double-recirculation zone, indicative of a transitional cavity flow. The separated mixing layer, indicated by the region of negative vorticity along $y/D \approx 0$ (wall-normal location of leading edge), can be seen to slightly lift away from the cavity floor at $x/D > 5$, under the influence of the rear vortex. In comparison, the baseline complex cavity (Fig. 7d), once again, shows only the single recirculation zone; this causes the mixing layer to curve slightly towards the floor of the cavity at $x/D > 4.5$, due to entrainment by the larger recirculation zone.

Along the span of the baseline complex cavity, the size and location of the recirculation zone varies little (Fig. 7f, h); however, at z/D = -1.38 (Fig. 7h), the mixing layer is seen to thicken and curve in towards the cavity floor to a greater degree than seen in the centerline. The rectangular cavity shows a different trend; at z/D = -0.72 (Fig. 7e), the second recirculation zone is no longer present, and the mixing layer itself appears to have dissipated past $x/D = 5$. Closer to the wall of the cavity (Fig. 7g, z/D = -1.38), the rear vortex returns.

III.C.2. Slices of wall-normal velocity (V)

The weakening of the mixing layer in Fig. 7 illustrates a degree of three-dimensionality that may be associated with edge effects. To investigate this further, contours of wall-normal velocity with in-plane velocity vectors are shown in Fig. 8, taken at three separate wall-normal locations (y/D = -0.50, 0, and 0.50). At y/D = -0.50, the rectangular cavity and the baseline complex cavity both appear to be rather two-dimensional. The small size of the velocity vectors is due to the location of the planes being within the region of reverse flow within the cavities. The rectangular cavity (Fig. 8c) has slight regions of negative velocity at $x/D \approx 5$ and positive at $x/D \approx 6$, which may represent recirculating flow associated with a spillage vortex. The baseline complex cavity (Fig. 8d) decreases from slightly positive values of wall-normal velocity to large negative values at $x/D > 6$; this is due to the recirculation zone within the baseline complex cavity, which directs flow towards the floor of the cavity.

At $y/D = 0$ (Fig. 8f), the baseline complex cavity shows little change, except for an increasingly larger region of negative velocity. The rectangular cavity, however shows an enlarged region of negative velocity, oriented at -1 $\leq z/D \leq$ -0.5, that extends almost across the entire length of the measurement domain. As seen in Fig. 7e, this is the spanwise region within which the secondary (downstream) recirculation zone within the rectangular cavity was no longer evident, and an apparent breakdown of the mixing layer was observed. The rectangular cavity flow at y/D = 0.50 (Fig. 8g) is outside of the cavity and above the separated mixing layer, leading to a nearly uniform flow.

The baseline complex cavity (Fig. 8h), on the other hand, continues to show increasingly negative values of velocity, oriented towards the rear corner of the cavity. Comparing to Fig. 7d, f, and h, it is apparent that this region of negative velocity corresponds to the downstream half of the baseline complex cavity recirculation zone. In addition, at y/D = 0.50, the region of negative velocity is concentrated towards the back corner of the cavity; as the back corner is approached, it may be that the recirculation zone within the cavity is experiencing a three-dimensional effect associated with the presence of the side wall.

Spanwise flow is directed from the side edge of the cavity towards centerline. This fact is illustrated better in Fig. 9, which re-presents the contours shown in Fig. 8e and h, using in-plane streamlines of U and $10\times W$. These two wall-normal locations correspond to $y/D = 0$ (Fig. 9a) and y/D = 0.50 (Fig. 9b), which correspond to wall-normal locations within the separated mixing layer for the two cavities. As is apparent in both cavity flows, the streamlines are vectored towards the centerline of the cavity, due to the streamwise velocity dominating over the spanwise velocity. This observation will be revisited later.

III.C.3. Slices of streamwise velocity (U)

To better represent the true three-dimensionality within the cavities, streamwise slices of U-velocity contours with in-plane vectors are shown in Fig. 10; these slices correspond to x/D = 3.5 (Fig. 10b, f), 4.5 (Fig. 10c, g), and 5.5 (Fig. 10d, h). Within the rectangular cavity, at x/D = 3.5 (Fig. 10b), the cavity flow appears relatively uniform along the span of the measurement domain. As mentioned previously, the measurement domain does not extend to the wall of the cavity. Closer to the wall of the cavity (z/D< -1), spillage can be seen entering into the cavity with a downward momentum. With increasing z/D towards the centerline of the rectangular cavity, there is first an acceleration of W (-0.4 < z/D < -1.38), followed by a deceleration as the centerline is approached. Further downstream at x/D = 4.5 (Fig. 10c), this effect is more pronounced, and an acceleration is also apparent in the streamwise velocity, centered around $z/D \approx$ -1. By x/D = 5.5 (Fig. 10d), the cavity flow located at -0.5 < z/D < -1 is nearly attached, as evidenced by the greatly reduced reverse flow within this region (it cannot be said that the flow is attached at this location since there is still some reverse flow present). This partial recovery within the cavity leads to the formation of a spanwise wavelength, which will be elaborated on in more detail shortly.

In comparison, the baseline complex cavity (Fig. 10f-h) demonstrates less three-dimensionality, albeit the mixing layer appears to tilt slightly towards the cavity floor as z/D with increasing distance from centerline.

In all three streamwise planes, there appears to be less of a tendency for the spillage from the side wall to enter into the cavity; rather a non-zero value of W-velocity appears to be localized around $y/D \approx 0.50$, the wall-normal location of the separated mixing layer. At $x/D = 3.5$ (Fig. 10f), this spillage resembles a vectored jet; as streamwise distance increases, this jet appears to weaken, possibly due to turbulent mixing. One peculiarity associated with the baseline complex cavity is the assymmetry apparent in Fig. 10f-h; the spanwise velocity does not appear to decelerate as the centerline is approached, but rather begins to form what appears to be a streamwise-oriented structure evidenced by an inflection point in the in-plane velocity vectors near y/D = -0.6, $0 \leq z/D \leq$ -0.5. Such a flow feature was noticed by Larchevêque et al.,[12] although no explanation of the cause was given. The presence of this vortical structure nearer centerline may be due to slight asymmetries within the turbulent boundary layer along the ramp upstream of the leading edge, which may create a net cross-flow, resulting in the formation of streamwise vorticity in the center plane. Similar secondary flow effects have been reported in the past for turbulent flow in ducts with and without massive separation.[24–26] This effect may not be noticed in the other complex geometries due to the presence of the scoop on the leading-edge ramp in those cases.

III.C.4. Streamwise vortex dynamics (ω_x)

Measurements collected using *SPIV* are limited to three-components of velocity and a single component of vorticity, ω_z, which is obtained from the in-plane velocity components. By performing a reconstruction of a volume within the cavity, it is possible to resolve the remaining two components of vorticity, ω_x and ω_y, as a spatial derivative in the z-direction is now possible. Figure 11 shows iso-contours of U-velocity for the rectangular cavity (Fig. 11a) and baseline complex cavity (Fig. 11b), along with iso-contours of streamwise vorticity, ω_x (Fig. 11c, d, respectively). The streamwise velocity volumes in Fig. 11 greatly resemble the iso-contours of V_{tot} shown in Fig. 6, which is expected considering that streamwise velocity dominates over the remaining two components. In the case of the streamwise vorticity, Fig. 11a shows that the rectangular cavity contains two major counter-rotating structures; a region of positive vorticity focused along the wall of the cavity that represents the spillage vortex, and a secondary structure of negative vorticity that runs along the cavity length, closer to the centerline. The wall-bounded region of positive vorticity grows in size with increasing streamwise distance, due to entrainment of flow. Likewise, the negative vortical structure appears to narrow downstream, possibly due to competing effects from the wall-bounded spillage vortex. Compared to this, the baseline complex cavity contains only a single structure of negative vorticity.

The two iso-contour volumes shown in Fig. 11a, c and b, d are superimposed on top of each other, as seen in Fig. 11e and f for the rectangular and baseline complex cavities, respectively. In both configurations, the regions of negative vorticity act primarily on the mixing layer; in the case of the rectangular cavity (Fig. 11e), the region identified in Fig. 10c, d where the mixing layer is brought closer to the cavity floor corresponds to the area that lies between the two vortical structures, resulting in the spanwise wavelength identified previously. A schematic of the streamwise-oriented vorticity is shown in Fig. 12a, c, and e for the rectangular cavity and Fig. 12b, d, and f for the baseline complex cavity. As shown in Fig. 9, a spanwise velocity entering the cavities from along the side walls vectors cavity flow towards the centerline. Because of this vectored flow (as seen in Fig. 12a, c), the vorticity shown in Fig. 11 is a projection in the y-z plane.

Flow enters the rectangular cavity due to the lack of pressure recovery within the cavity. As the flow separates at the sharp side edge, it creates streamwise vorticity that acts to bring high momentum flow from the freestream into the cavity (Fig. 12e). This positive vortical motion induces a secondary vortical structure of equal and opposite strength that rotates closer to the centerline, which also increases mixing and transfers momentum from the freestream into the cavity. The combined induced velocity (seen in Fig. 8e) from the two vortical structures pushes the mixing layer down (Fig. 10c, d), weakening the mixing layer emanating from the leading edge (Fig. 7e), and suppressing the formation of the rear vortex.

The formation of the pair of counter-rotating vortices, i.e. a spillage vortex along the wall and an induced secondary vortex, are qualitatively similar to the computational results of Ohmichi & Suzuki,[27] who showed the formation of this same vortex pair within a shallow, finite-span cavity in hypersonic conditions, and Dudley & Ukeiley,[14] who observed these structures at $x/D = 3.0$. Arunajatesan et al.[19] showed that the induced secondary vortex is associated with sufficiently wide cavities, whereas if the cavity is too narrow, only the spillage vorticies will exist. In addition, Crook et al.[18] also visualized the formation of these structures experimentally in low-speed subsonic flows using *PIV*.

In comparison, the baseline complex cavity (Fig. 11b, d, and f) shows little vorticity penetrating through the mixing layer. This structure in the baseline complex cavity rotates with a sense that curves the mixing

layer in towards the floor of the cavity as the wall of the cavity is approached. One question that arises is why the baseline complex cavity seemingly lacks a spillage vortex along this wall. Spanwise flow is drawn into the cavity due to a low pressure within the cavity associated with a lack of pressure recovery. Recall that the baseline complex cavity is formed from the addition of side ramps; in the spanwise direction, flow entering the cavity travels up a ramp at a 26.6° incline, i.e. it is accelerated due to a favorable pressure gradient, which reduces the local pressure at the edge (Fig. 12b). At the ramped edge, the decreased local pressure results in a reduced pressure difference between then cavity edges and floor, in comparison to the rectangular cavity case. The momentum of the spanwise flow is now enough to resist the reduced pressure difference and instead is entrained into the separated mixing layer (Fig. 12d, f). As was seen in Fig. 10f - h, this results in the spanwise flow behaving like a vectored jet, where the streamwise vorticity shown in Fig. 11 is representative of the jet shear.

IV. Conclusions

The subsonic flow within a series of finite-span cavities of varying geometry was measured experimentally using stereoscopic particle image velocimetry (*SPIV*), to resolve the three components of velocity along the center plane. Using this technique, it was possible to visualize the large recirculation zone that exists within each of these cavities, classifying them as open, closed, or transitional. The open cavity is typically associated with an aspect ratio, $L/D <$ 6-8; however the exact effective aspect ratio for the various complex geometries is not always clear due to the physical differences between them and a rectangular cavity. Furthermore, the rectangular cavity case has a transitional flow field, which results in the formation of two distinct recirculation zones.

SPIV measurements were repeated at 17 planes along the spanwise direction, beginning at centerline and traversing towards the wall, in 2-4 mm increments. From these data, it was possible to resolve volumes representing the flow within two of the cavities: rectangular and baseline complex. The rectangular cavity flow field was affected by spillage issuing from along the side walls, drawn into the cavity. This spillage resulted in the formation of a spillage vortex, which induced a secondary structure, modifying the shape of the mixing layer. In contrast, the ramps of the baseline complex cavity accelerated the spanwise fluid velocity, which prevented spillage into the cavity. This resulted in the baseline complex cavity having a more two-dimensional mixing layer compared to the rectangular cavity. Future work will reconstruct volumes within the remaining complex cavity geometries to investigate how their various geometric differences may also impact the formation of streamwise vorticity and relate changes to the flow structure to the frequency and amplitude of the resonances.

Acknowledgments

The authors would like to thank Thomas Grasser for his help in the designing of the experimental hardware and Dr. Katya M. Casper for indispensable guidance in the graphical design of the figures.

References

[1]Tracy, M.B., and Plentovich, E.B., "Cavity unsteady-pressure measurements at subsonic and transonic speeds," NASA Technical Paper 3669, Dec. 1997.

[2]Rossiter, J.E., "Wind-tunnel experiments on the flow over rectangular cavities at subsonic and transonic speeds," Aeronautical Research Council Reports and Memoranda No. 3438, Oct. 1964.

[3]Coley, C.J., and Lofthouse, A.J., "Correlation of weapon bay resonance and store unsteady force and moment loading," AIAA Paper 2012-0415, Jan. 2012.

[4]Wagner, J.L., Casper, K.M., Beresh, S.J., Hunter, P.S., Spillers, R.W., Henfling, J.F., and Mayes, R.L., "Fluid-structure interactions in compressible cavity flows," *Physics of Fluids* Vol. 27, 2015, pp. 1-20.
doi: 10.1063/1.4922021.

[5]Heller, H.H., and Bliss, D.B., "The physical mechanism of flow-induced pressure fluctuations in cavities and concepts for their suppression," AIAA Paper 75-491, March 1975.
doi: 10.2514/6.1975-491.

[6]Dix, R.E., and Bauer, R.C., "Experimental and predicted acoustic amplitudes in a rectangular cavity," AIAA Paper 2000-0472, Jan. 2000.
doi: 10.2514/6.2000-472.

[7]Casper, K.M., Wagner, J.L., Beresh, S.J., Henfling, J.F., Spillers, R.W., and Pruett, B.O.M., "Complex geometry effects on cavity resonance,"*AIAA Journal*, published online 7 Sept. 2015; also AIAA Paper 2015-1291, Jan. 2015.

doi: 10.2514/1.J054273.

[8]Ahuja, K.K., and Mendoza, J., "Effects of cavity dimensions, boundary layer, and temperature on cavity noise with emphasis on benchmark data to validate computational aeroacoustic codes," NASA CR-4653, April 1995.

[9]Disimile, P.J., Toy, N., and Savory, E., "Effect of planform aspect ratio on flow oscillations in rectangular cavities," *Transactions of the ASME*, Vol. 122, 2000, pp. 32-38.

[10]Hein, S., Koch, W., and Schoberl, J., "Acoustic resonances in a 2D high lift configuration and 3D open-cavity," AIAA Paper 2005-2867, May 2005.
doi: 10.2514/6.2005-2867.

[11]Woo, C., Kim, J., and Lee, K., "Three-dimensional effects of supersonic cavity flow due to the variation of cavity aspect and width ratios," *Journal of Mechanical Science and Technology*, Vol. 22, 2008, pp. 590-598.
doi: 10.1007/s12206-007-1103-9.

[12]Larchevêque, L., Sagaut, P., and Labbe, O., "Large-eddy simulation of a subsonic cavity flow including asymmetric three-dimensional effects," *Journal of Fluid Mechanics*, Vol. 577, 2007, pp. 105-126.
doi: 10.1017/S0022112006004502.

[13]Brès, G.A., and Colonius, T., "Three-dimensional instabilities in compressible flow over open cavities," *Journal of Fluid Mechanics*, Vol. 599, 2008, pp. 309-339.
doi: 10.1017/S0022112007009925.

[14]Dudley, J.G., and Ukeiley, L., "Detached eddy simulation of a supersonic cavity flow with and without passive flow control," AIAA Paper 2011-3844, June 2011.
doi: 10.2514/6.2011-3844.

[15]Wagner, J.L., Casper, K.M., Beresh, S.J., Henfling, J.F., Spillers, R.W., Pruett, B.O., "Mitigation of wind tunnel wall interactions in subsonic cavity flows," *Experiments in Fluids*, 2015, pp. 56-59.
doi: 10.1007/s00348-015-1924-8.

[16]Beresh, S.J., Wagner, J.L., Pruett, B.O.M., Henfling, J.F., and Spillers, R.W., "Supersonic flow over a finite-width rectangular cavity," *AIAA Journal*, Vol. 53, No. 2, 2015, pp. 296-310; also AIAA Paper 2013-0389, Jan. 2013.
doi: 10.2514/1.J053097.

[17]Beresh, S.J., Wagner, J.L., Henfling, J.F., Spillers, R.W., Pruett, B.O.M., "Width effects in transonic flow over a rectangular cavity," *AIAA Journal*, Vol. 53, No. 12, 2015, pp. 3831-3834.
doi: 10.2514/1.J054362.

[18]Crook, S.D., Lau, T.C.W., and Kelso, R.M., "Three-dimensional flow within shallow, narrow cavities," *Journal of Fluid Mechanics*, Vol. 735, 2013, pp. 587-612.
doi: 10.1017/jfm.2013.519.

[19]Arunajatesan, S., Barone, M.F., Wagner, J.L., Casper, K.M., and Beresh, S.J., "Joint experimental/computational investigation into effects of finite width on transonic cavity flow," AIAA Paper 2014-3027, June 2014.
doi: 10.2514/6.2014-3027.

[20]Murray, N., Sallstrom, E., and Ukeiley, L., "Properties of subsonic open-cavity flow fields," *Physics of Fluids*, Vol. 21, 2009, pp. 1-16.
doi: 10.1063/1.3210772.

[21]Haigermoser, C., Scarano, F., Onorato, M., "Investigation of the flow in a rectangular cavity using tomographic and time-resolved PIV," 26th International Congress of the Aeronautical Sciences, Paper ICAS 2008-3.2.2, Sept. 2008.

[22]Haigermoser, C., Scarano, F., Onorato, M., "Investigation of the flow in a circular cavity using stereo and tomographic particle image velocimetry," *Experiments in Fluids*, Vol. 46, 2009, pp. 517-526.
doi: 10.1007/s00348-008-0577-2.

[23]Zhuang, N., Alvi, F.S., Alkislar, M.B., and Shih, C., "Supersonic cavity flows and their control," *AIAA Journal*, Vol. 44, No. 9, 2006, pp. 2118-2128.
doi: 10.2514/1.14879.

[24]Gartner, J., and Amitay, M., "Effect of boundary layer thickness on secondary structures in a short inlet curved duct," *International Journal of Heat and Fluid Flow*, Vol. 50, 2014, pp. 467-478.
doi: 10.1016/j.ijheatfluidflow.2014.10.016.

[25]Perkins, H.J., "The formation of streamwise vorticity in turbulent flow," *Journal of Fluid Mechanics*, Vol. 44, part 4, 1970, pp. 721-740.

[26]Bradshaw, P., "Turbulent secondary flows," *Annual Review of Fluid Mechanics*, Vol. 19, 1987, pp. 53-74.

[27]Ohmichi, Y., and Suzuki, K., "Flow structure and heating augmentation around finite-width cavity in hypersonic flow," *AIAA Journal*, Vol. 52, No. 8, 2014, pp. 296-310; also AIAA Paper 2011-3966, June 2011.
doi: 10.2514/1.J052647.

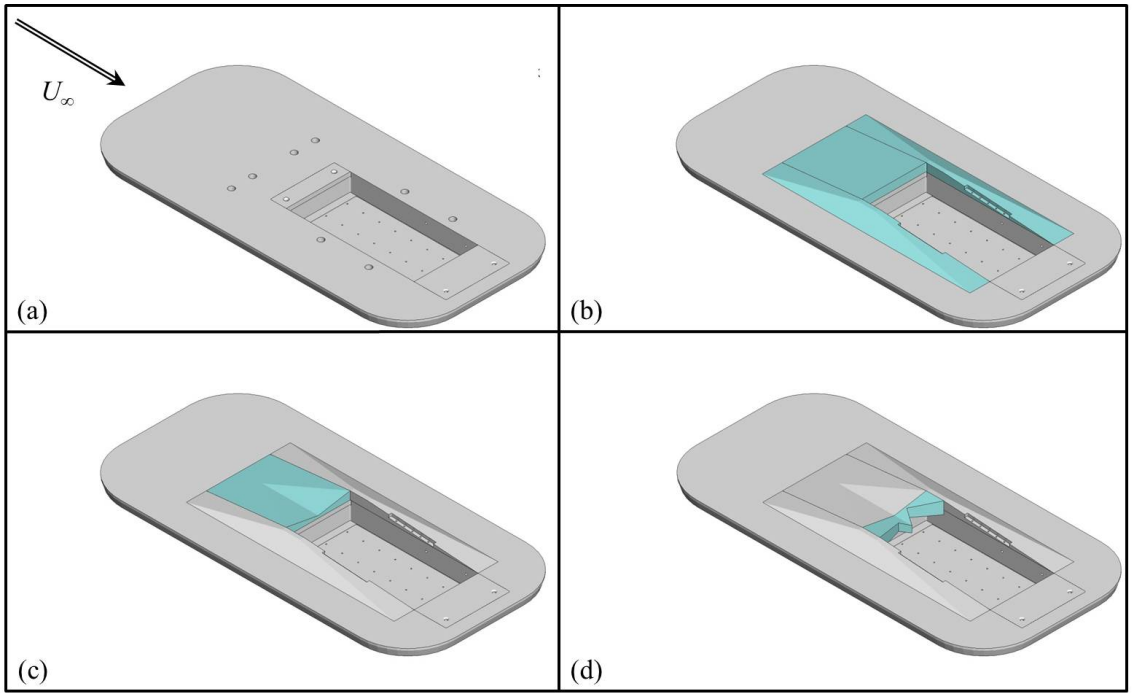

Figure 1. Geometric modification of the rectangular cavity resulting in the complex geometries tested: (a) rectangular cavity; (b) baseline complex cavity; (c) center scoop complex cavity; (e) center scoop complex cavity with tooth. Blue color indicates the feature added to make a given configuration.

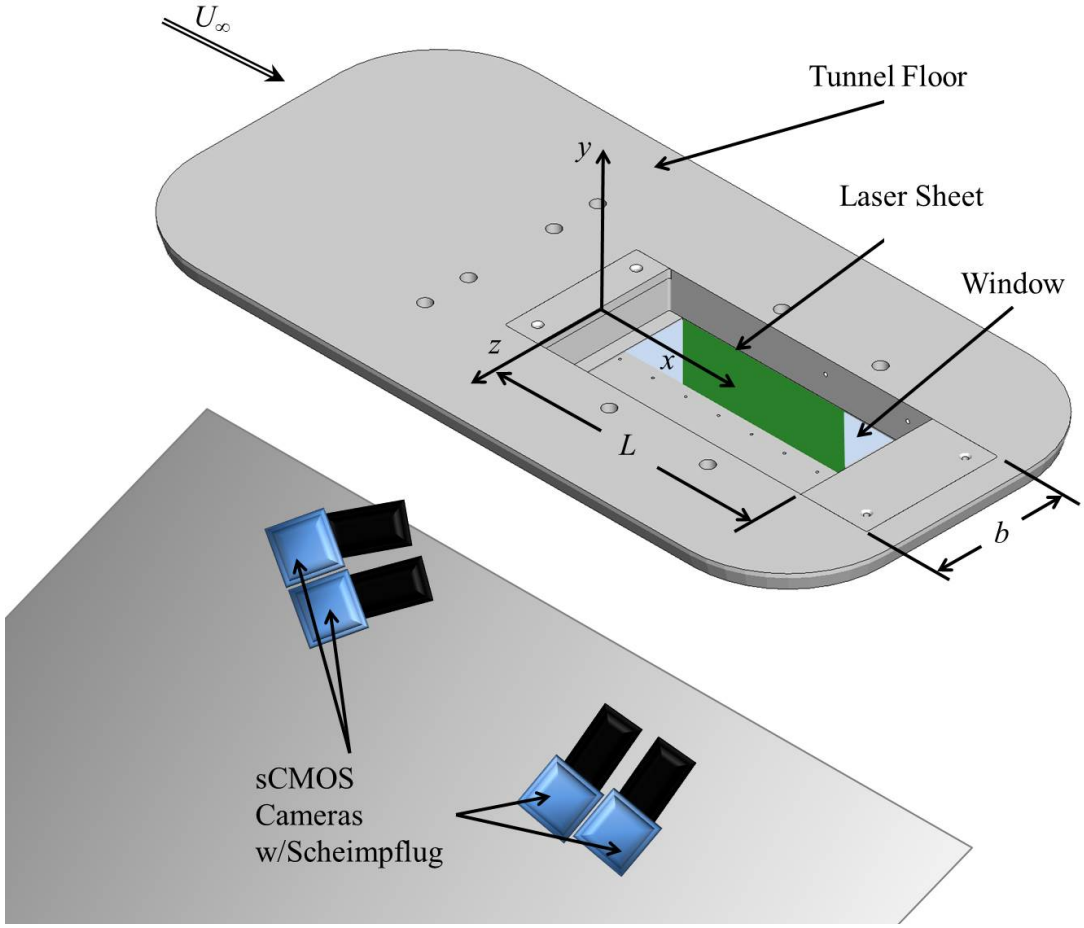

Figure 2. Location of the measurement plane with respect to the (rectangular) cavity. The axis origin is located midway on the leading edge of the cavity. The upper surface, indicated by the arrow, identifies the surface of the tunnel floor. Note that D (not shown) is the cavity depth, along the y-direction.

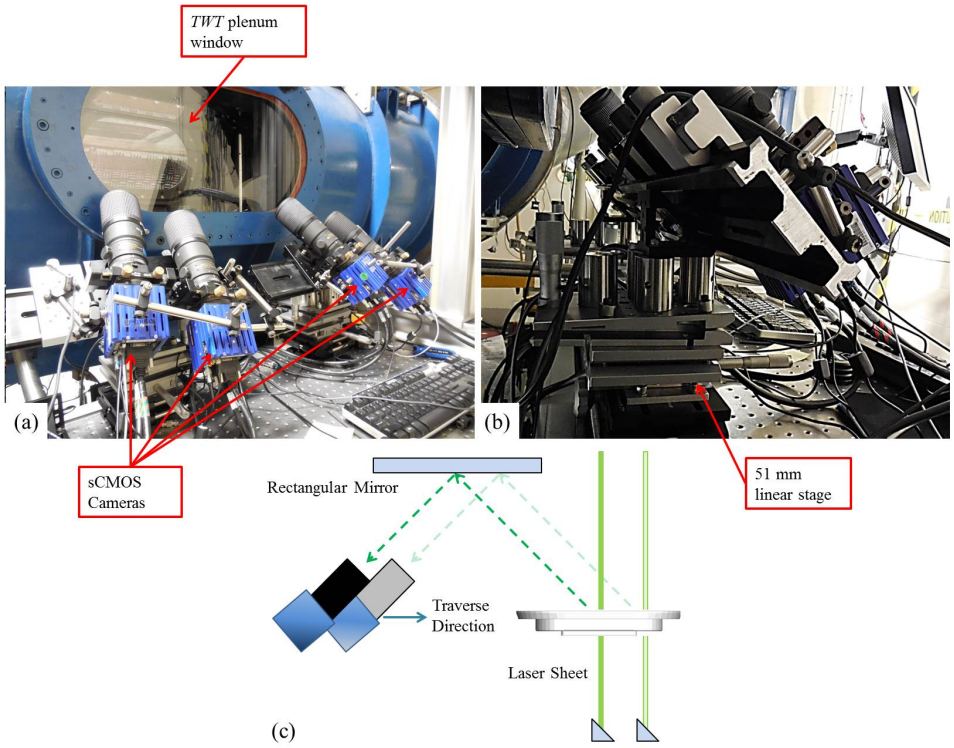

Figure 3. Photographs and schematic of the data collection procedure: (a) cameras mounted at a tilt angle for optical access; (b) traversing of the cameras using a 51 mm linear translation stage; (c) schematic of how imaging of the cavity flow field was achieved.

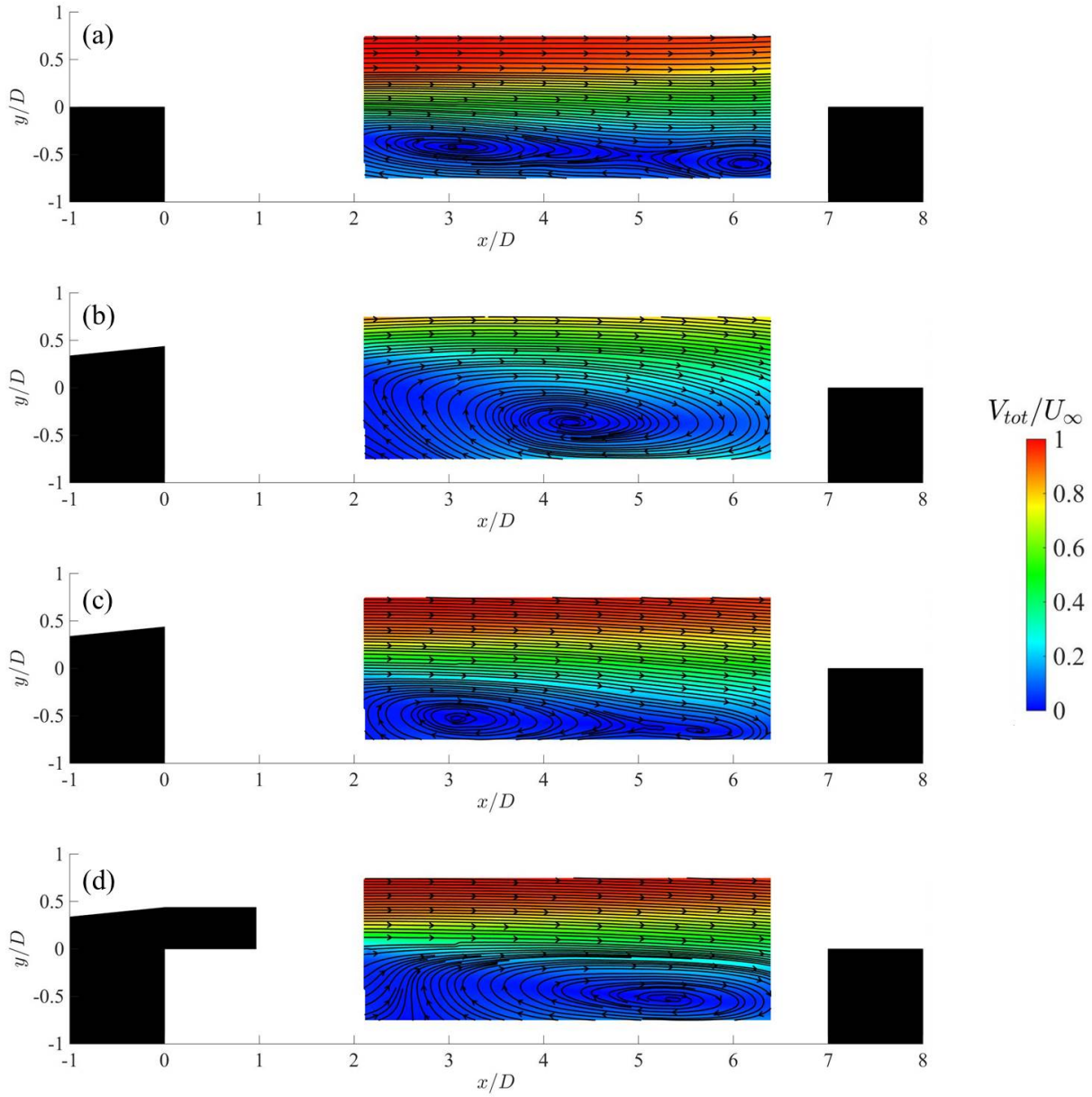

Figure 4. Color contours of total velocity (V_{tot}) with in-plane streamlines for four cavity configurations at $x/D = 0$: (a) rectangular cavity; (b) baseline complex cavity; (c) center scoop cavity; (d) center scoop with tooth. The black boxes represent the edges of each respective cavity, for purposes of scale.

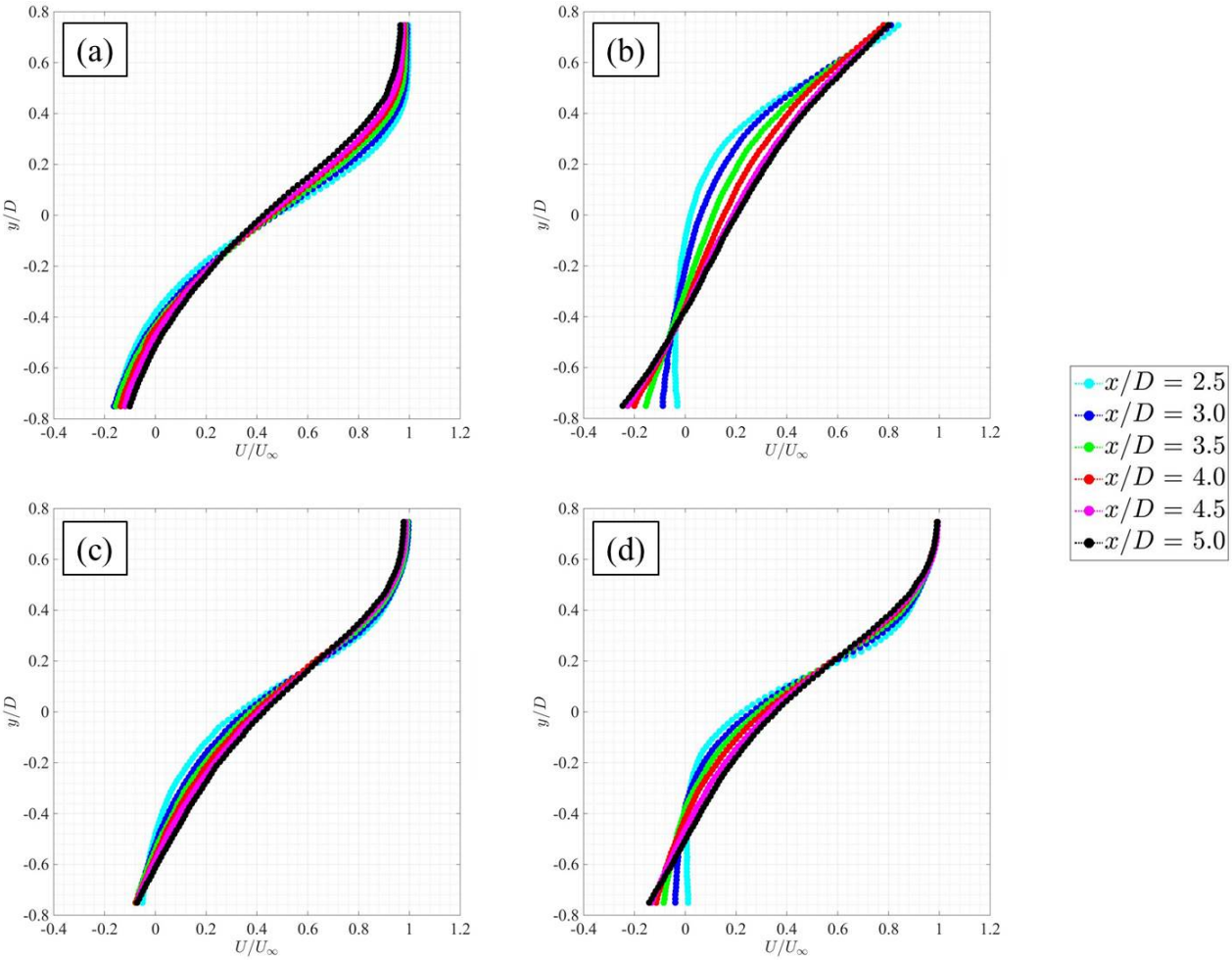

Figure 5. Wall-normal distributions of streamwise velocity, (U) at several streamwise locations along the length of the cavity: (a) rectangular cavity; (b) baseline complex cavity; (c) center scoop complex cavity; (e) center scoop complex cavity with tooth.

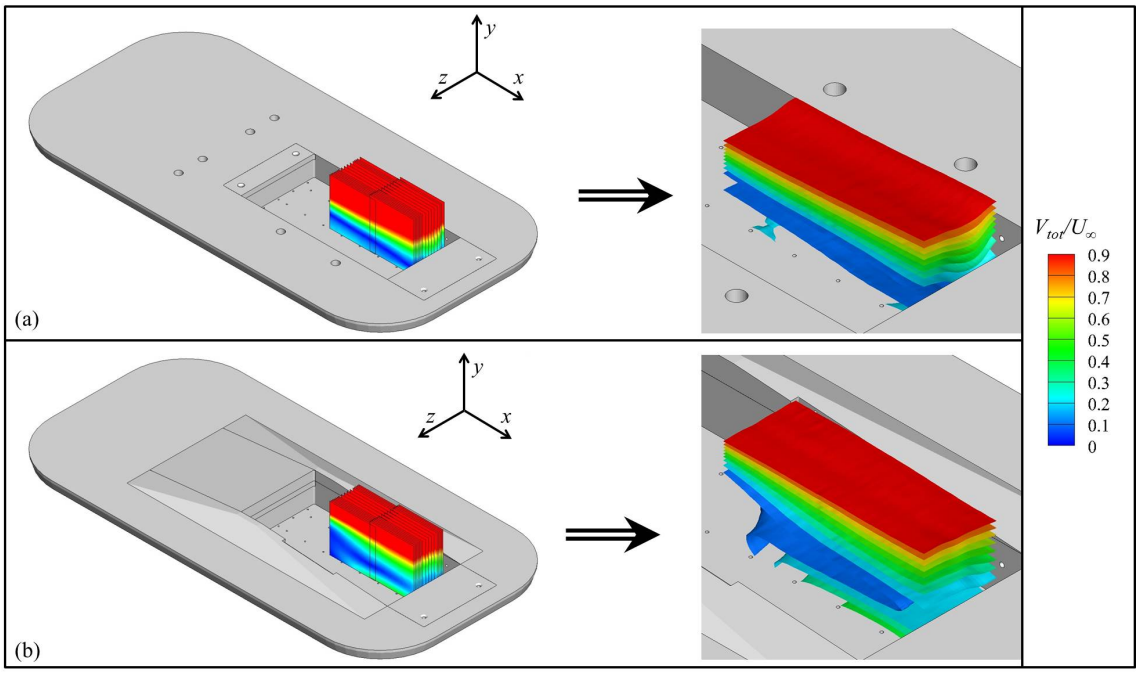

Figure 6. The volumes were reconstructed from planes measured at 17 spanwise locations, for the rectangular (a) and baseline complex (b) cavities. Note the orientation of the freestream velocity with respect to the cavities.

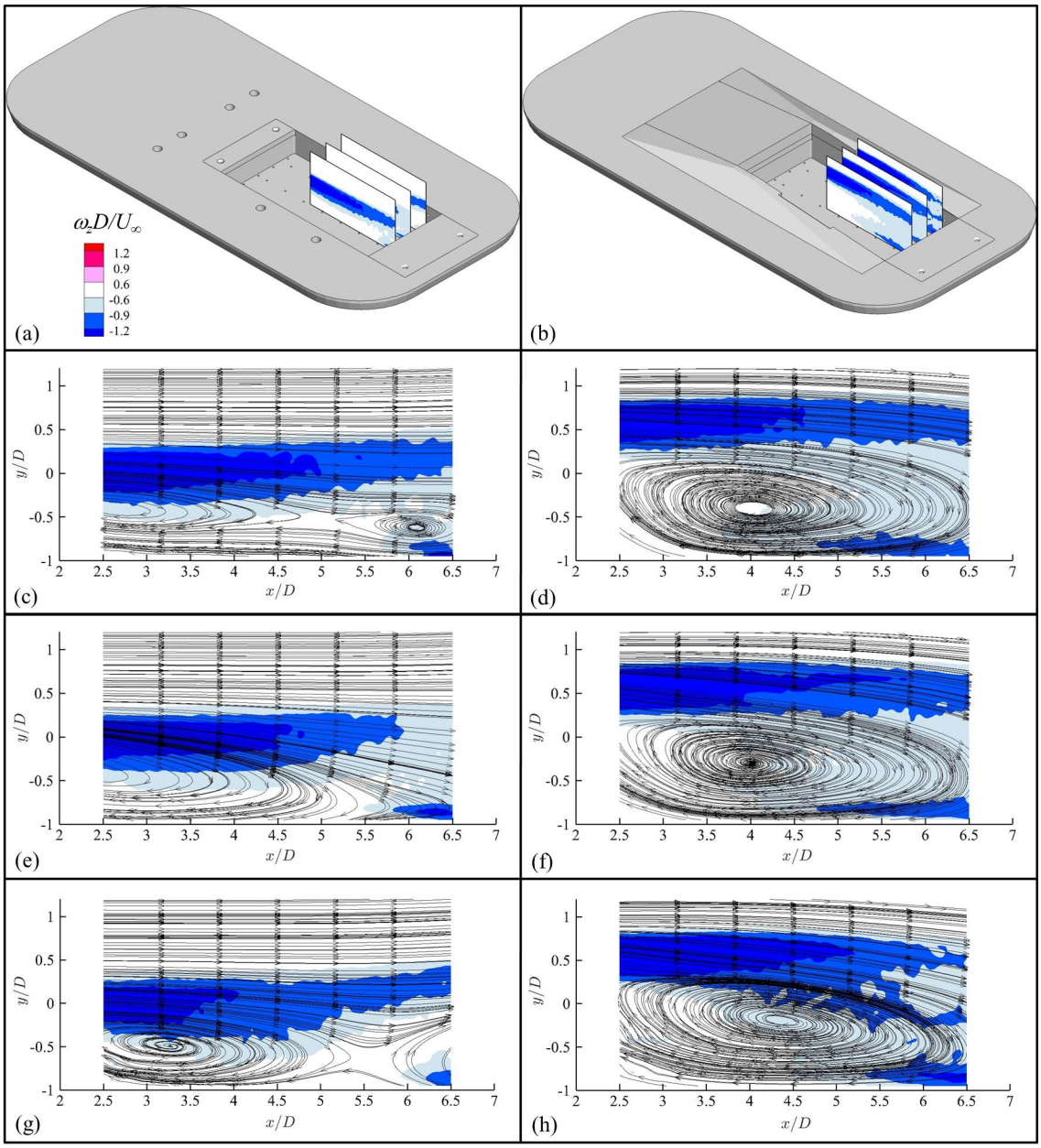

Figure 7. Contours of spanwise vorticity (ω_z) with in-plane streamlines, within the reconstructed volume; rectangular cavity (a, c, e, g) and baseline complex cavity (b, d, f, h): (a, b) location of slices within volume; z/D = (c, d) 0, (e, f) -0.72; (g, h) -1.38.

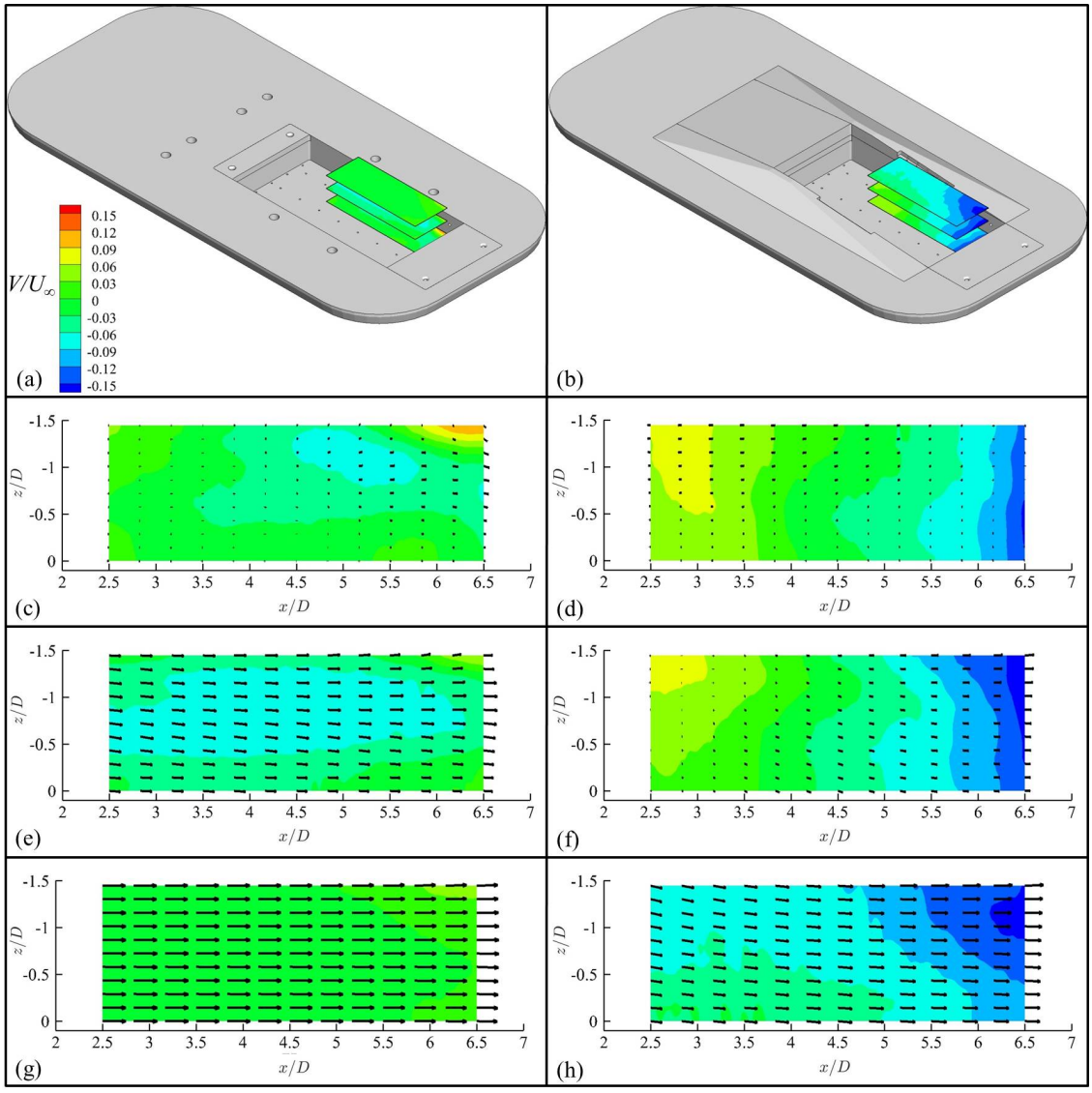

Figure 8. Contours of wall-normal velocity (V) with in-plane vectors, within the reconstructed volume; rectangular cavity (a, c, e, g) and baseline complex cavity (b, d, f, h): (a, b) location of slices within volume; y/D = (c, d) -0.50, (e, f) 0 (g, h) 0.50.

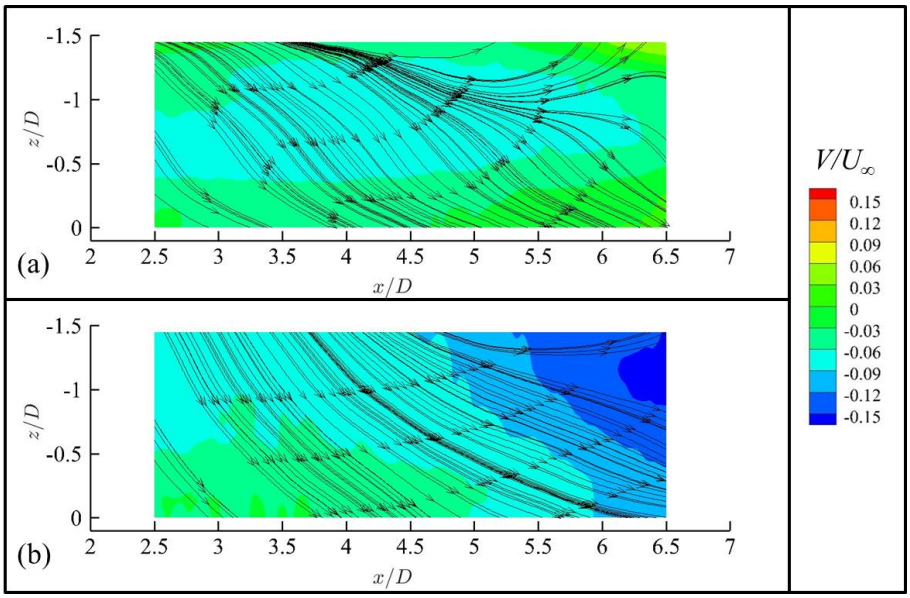

Figure 9. Contours of wall-normal velocity taken at the approximate location of the center of the separated mixing layer, y/D = (a) 0 (rectangular cavity) and (b) 0.50 (baseline complex cavity). The images have been superimposed with in-plane streamlines of U and $10\times W$, in order to highlight the inflow towards the cavity centerline.

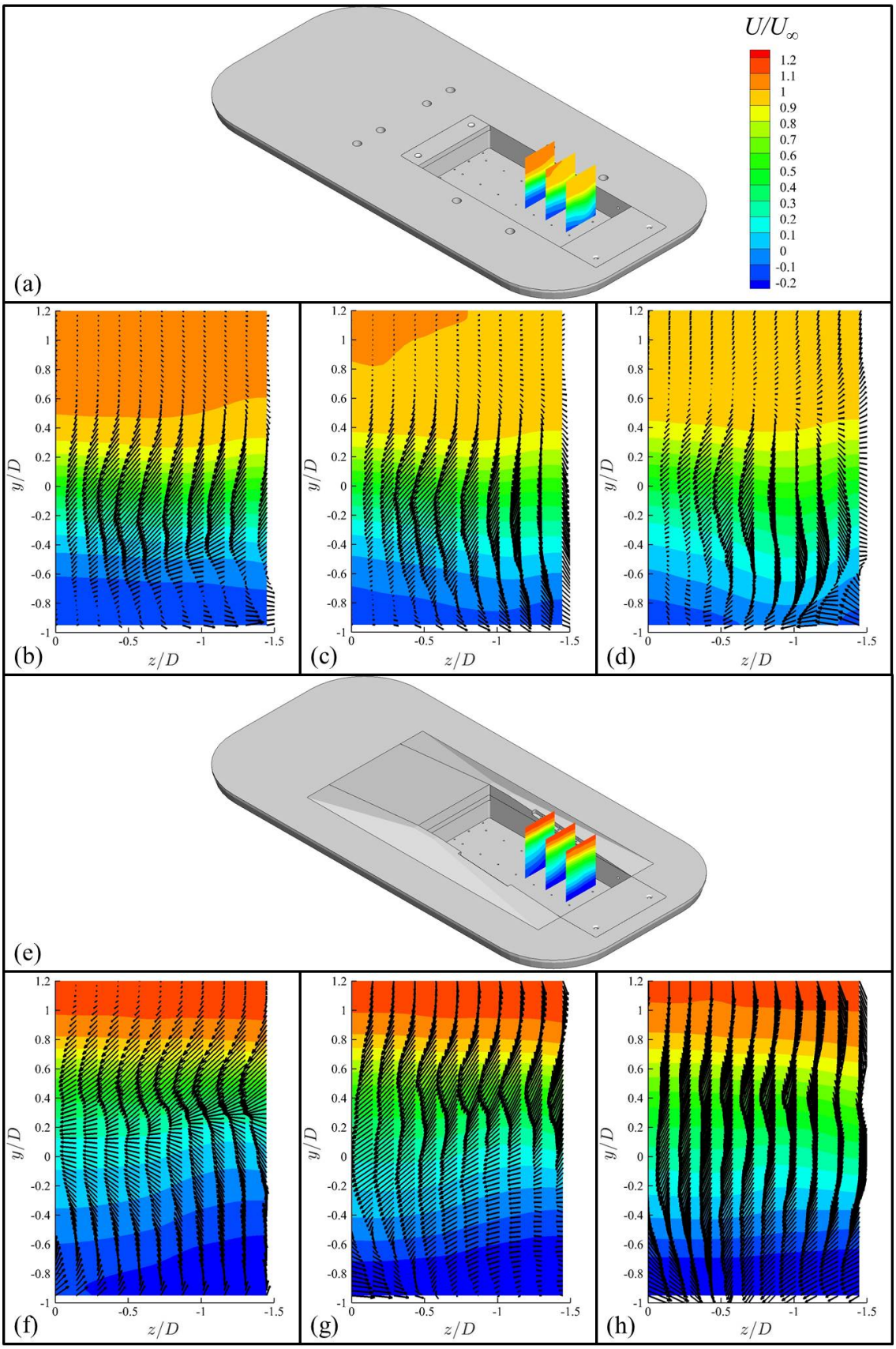

Figure 10. Contours of streamwise velocity (U) with in-plane vectors, within the reconstructed volume; rectangular cavity (a-d) and baseline complex cavity (e-h): (a, e) location of slices within volume; x/D = (b, f) 3.5, (e, f) 4.5 (g, h) 5.5.

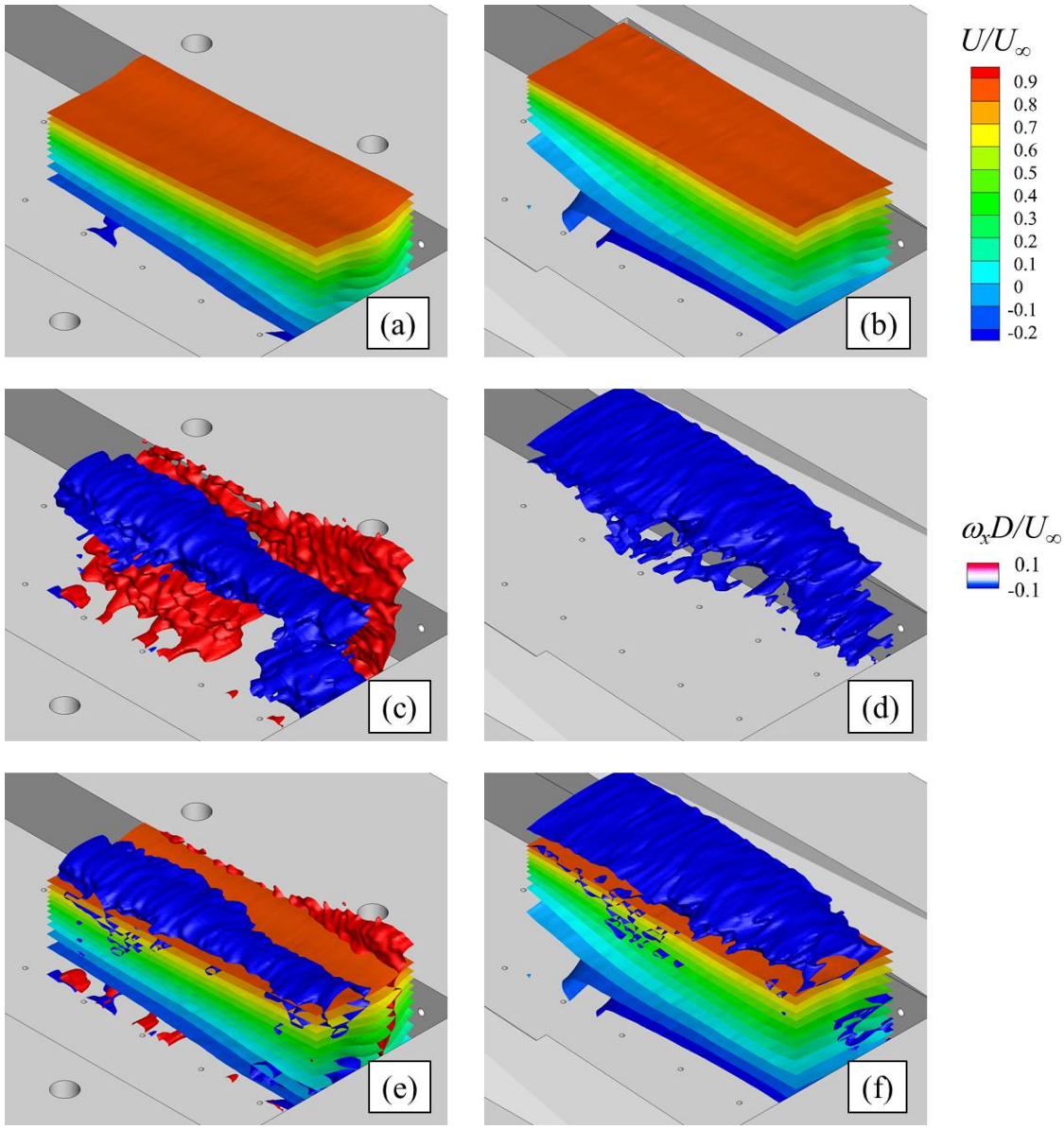

Figure 11. Iso-contours of streamwise velocity (U) for the rectangular (a) and baseline complex cavity (b); iso-contours of streamwise vorticity (ω_x) for the rectangular cavity (c) and the baseline complex cavity (c); the velocity iso-contours superimposed with the streamwise vorticity for the rectangular cavity (e) and the baseline complex cavity (f). The vorticity iso-contours for the baseline complex cavity are only showing values of negative vorticity in order to highlight the relevant coherent structure.

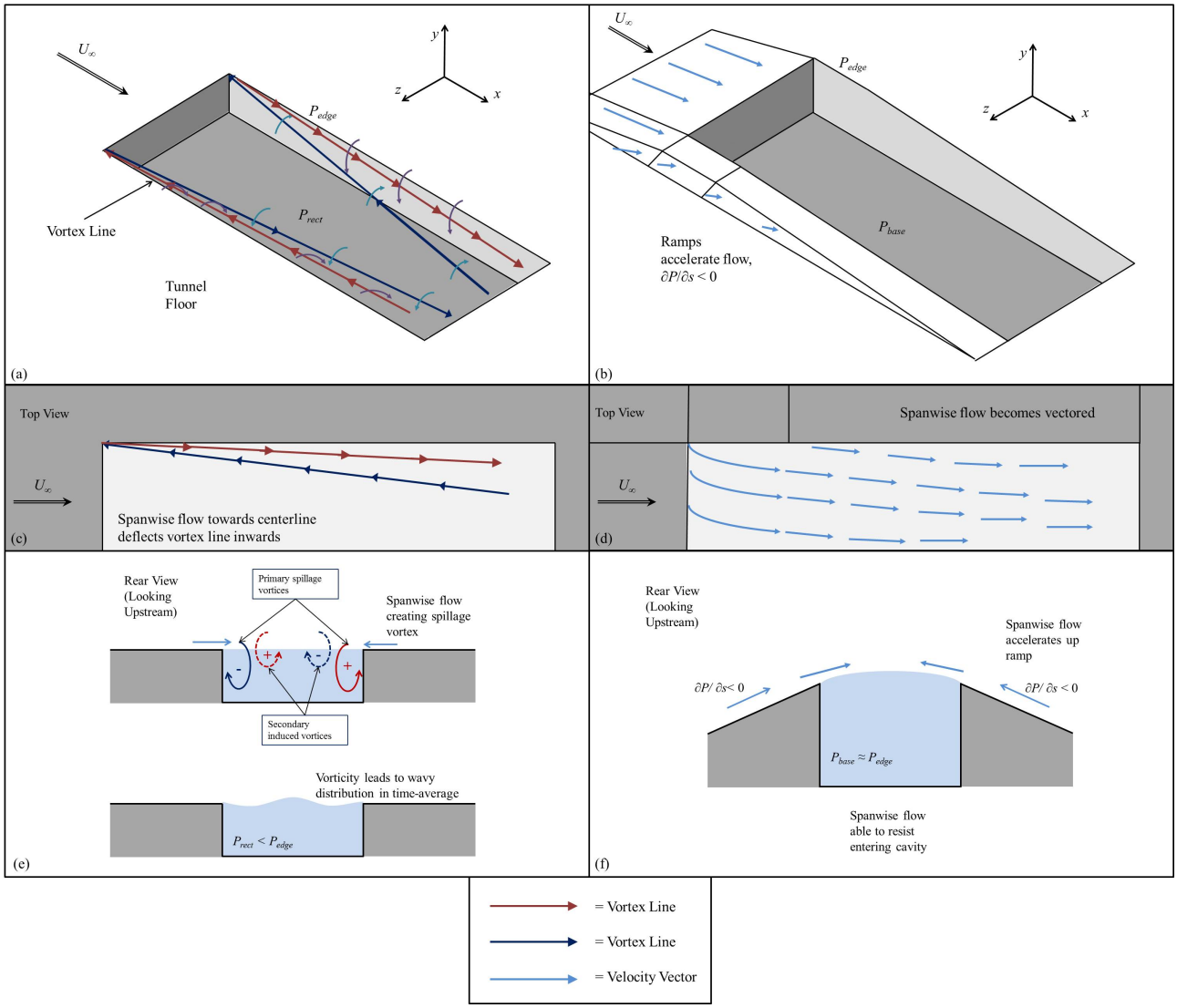

Figure 12. Schematic spanwise effects associated with rectangular cavity and baseline complex cavity: (a) Vortex represent the cores of the vortices observed within the rectangular cavity; (b) ramps of the baseline complex cavity accelerate flow; (c) spanwise flow towards centerline (Fig. 9a) deflects vortex lines in rectangular cavity; (d) flow does not penetrate mixing layer to same extent in baseline complex cavity, not resulting in spillage vortex; (e) the pattern of spillage and induced vortices in rectangular cavity leads to spanwise waviness within the mixing layer; (f) because spanwise flow is accelerated in baseline complex cavity, it can better withstand low-pressure region inside cavity, resulting in a more two-dimensional mixing layer. Note that $\partial P/\partial s$ refers to the pressure gradient in the tangential direction to the flow.